ROYAL SOCIETY OF CHEMISTRY

PAPER

Check for updates

Role of the electron transport layer in dictating the nanoscale heterogeneity in all-inorganic perovskite absorbers – correlating the optoelectronic and crystallographic properties†

Stefan Nicholson, [ID] [ab] Jochen Bruckbauer, [ID] [b] Paul R. Edwards, [b] Carol Trager-Cowan, [b] Robert W. Martin[b] and Aruna Ivaturi [ID] *[a]

Within the field of perovskite photovoltaics, there has been heavy focus on either improving the conductivity/mobility of the charge transport layers [electron transport (ETL) or hole transport layers (HTL)], or tuning their energy alignment with the perovskite absorber for optimising the device efficiency, with little attention paid to the impact of the underlying charge transport layer on the structural and optoelectronic properties of the perovskite overlayer. For example, in the n–i–p device architecture, the ETL provides a key surface upon which the perovskite film grows. In this work, electron backscatter diffraction (EBSD) and cathodoluminescence (CL) spectroscopy are used to show a direct correlation between optical emission and structural properties of all-inorganic $CsPbI_2Br$ perovskite absorber thin films with a selection of inorganic underlying ETLs, giving insights into the vital role of the ETL. Comparisons are drawn between the effect of three commonly used electron transport layers (zinc oxide, titanium dioxide and tin oxide) on the optical emission and crystallographic properties of the $CsPbI_2Br$ perovskite thin films processed at two different annealing temperatures. Among the ETLs, zinc oxide is found to promote perovskite films with enhanced grain size and preferred growth along the [100] orientation, and relatively uniform light emission for the high temperature processed layer, showing its strong potential as a low-cost electron transport layer for the development of perovskite solar cells. Titanium dioxide is found to result in a high level of heterogeneity in the light emission when the perovskite is processed at low temperature, while tin oxide is found not to promote large grain growth. The observed variations are understood in terms of the differences in thermal expansion coefficient of the perovskite as compared to those of the ETLs as well as the leading strain in the lattice. The results from the study show the importance of considering perovskite growth effects when selecting an underlayer.

Introduction

The use of metal halide perovskites as solar absorber materials has gained significant attention in recent years, with nearly 1200 articles published in the first 3 months of 2024 alone.[1] There is a drive towards achieving high efficiency and long-lifetime devices, while minimising manufacturing cost. Long-term stability is enhanced by improving absorber materials through dopants and by employing encapsulants, while cost reduction is achieved by improving deposition methods and

[a]Smart Materials Research and Device Technology Group, Department of Pure and Applied Chemistry, University of Strathclyde, Glasgow G1 1XL, UK. E-mail: aruna. ivaturi@strath.ac.uk

[b]Semiconductor Spectroscopy and Devices Group, Department of Physics, SUPA, University of Strathclyde, Glasgow G4 0NG, UK

† Electronic supplementary information (ESI) available. See DOI: https://doi.org/10.1039/d4ta07152b

reducing annealing temperatures. In the pursuit of high efficiency devices, hybrid metal halide perovskites such as methylammonium lead iodide (MAPI) or formamidinium lead iodide (FAPI) have been extensively researched. A record power conversion efficiency (PCE) of 25.8% has been achieved using FAPI, thanks to the ideal and tunable bandgap.[2] However, these cells face temperature, moisture and oxygen-induced degradation issues due to volatile organic components of the absorber layer.[3–5] Among the various perovskite materials, $CsPbI_2Br$ has garnered particular interest due to its useful bandgap of 1.9 eV, enabling both sunlight and indoor light harvesting.[6] It also has great potential for use as absorber material in silicon-perovskite tandem solar cells, with a theoretically predicted PCE of over 31%.[7] $CsPbI_2Br$ has distinct advantages over organometal mixed halide perovskites due to improved heat stability than other all-inorganic materials, for example $CsPbI_3/CsPbBr_3$. While $CsPbI_3$ has a suitable bandgap of 1.73 eV, it suffers from

Table 1 CsPbI$_2$Br based solar cell structures exhibiting high efficiencies with the respective ETLs and perovskite annealing conditions reported in literature

ETL (ref.)	Device structure	PCE	Dopant/treatment used	Perovskite annealing method	ETL annealing method
TiO$_2$ [12]	FTO/TiO$_2$/CsPbI$_2$Br/spiro-MeOTAD/Ag	16.5%	Methyl urea at 0.9 mg mL^{-1} in perovskite precursor	100 °C for 3 min, 160 °C for 10 min	From TiCl$_4$ 70 °C for 1 hour, 100 °C for 10 min
TiO$_2$ [13]	FTO/TiO$_2$/CsPbI$_2$Br/spiro-MeOTAD/Ag	16.0%	Acetone/DMSO mixed solvent for precursor	40 °C for 5 min, 150 °C for 5 min	From TiCl$_4$ 70 °C for 1 hour, 150 °C for 1 hour
TiO$_2$ [14]	ITO/TiO$_2$/CsPbI$_2$Br/spiro-MeOTAD/Au	16.1%	IPA antisolvent treatment	50 °C for 1 min, 100 °C for 1 min, 160 °C for 10 min	From titanium isopropoxide (TTIP) spin coating 150 °C for 30 min
TiO$_2$ [15]	FTO/TiO$_2$/CsPbI$_2$Br/P3HT/Ag	17.5%	[BMIM]PF$_6$ in perovskite precursor	43 °C for 3 min, 160 °C for 10 min	From titanium isopropoxide (TTIP) spin coating 500 °C for 45 min
TiO$_2$ [16]	FTO/c-TiO$_2$/mp-TiO$_2$/M:CsPbI$_2$Br/P3HT/Au	17.5%	InCl$_3$ in perovskite precursor	280 °C for 10 min	From titanium isopropoxide (TTIP) 450 °C for 30 min Mesoporous at 500 °C for 15 min
SnO$_2$ [17]	ITO/SnO$_2$/CsPbI$_2$Br/PCBM/Ag	16.8%	NMP 2.5% in perovskite precursor	40 °C for 3 min, 160 °C for 10 min	Nanoparticles 150 °C for 30 min
SnO$_2$ [18]	ITO/SnO$_2$/CsPbI$_2$Br/spiro/Au	16.4%	CsBr post-treatment of film	25 °C for 15 min, 280 °C for 10 min	Nanoparticles 150 °C for 30 min
SnO$_2$ [19]	ITO/SnO$_2$/CsPbI$_2$Br/polyDTSTPD-r-BTbTPD/Au	15.5%	Aged ETL solution	RT for 10 min, 180 °C for 10 min	From SnCl$_2$ 100 °C for 10 min, 180 °C for 1 hour
ZnO [20]	ITO/SnO$_2$/ZnO/CsPbI$_2$Br/PTAA/MoO$_3$/Ag	16.2%	BMIMPF6 0.15% in perovskite precursor	250 °C for 10 min	From ZnAc sol–gel, 200 °C for 20 min
ZnO [21]	ITO/ZnO/CsPbI$_2$Br/spiro/Au	14.3%	GABr post-treatment	40 °C to 140 °C 10 min	From ZnAc sol–gel, 150 °C for 30 min
ZnO [22]	FTO/ZnO/CsPbI$_2$Br/PM6/MoO$_3$/Ag	16.4%	Pb(ac)$_2$ in ETL precursor	45 °C for 1 min, 160 °C for 5 min	From ZnAc sol–gel, 150 °C for 30 min
ZnO [23]	ITO/ZnO/CsPbI$_2$Br/PC$_{61}$BM/Ag	16.8%	ZnAc in ETL precursor	50 °C for 30 s, 240 °C for 60 s	From ZnAc sol–gel, 150 °C for 30 min

11004 | *J. Mater. Chem. A*, 2025, **13**, 11003–11014

This journal is © The Royal Society of Chemistry 2025

rapid moisture-induced degradation to a non-photoactive phase.[8] In contrast, $CsPbBr_3$ is more stable but has a bandgap of 2.3 eV which is not ideal for an efficient single-junction solar cell.[9] The $CsPbI_2Br$ mixed-halide material offers the best of both worlds.

Perovskite solar cells can be fabricated in different configurations: p–i–n or n–i–p, both of which can be planar or mesoscopic. The n–i–p architecture generally consists of a bottom electrode made from a fluorine-doped tin oxide layer (FTO) on glass, followed by an electron transport layer (ETL) such as SnO_2, TiO_2, ZnO *etc.*, the perovskite absorber, a hole transporting layer (HTL) like spiro-OMeTAD and a metal electrode on top. In contrast, p–i–n cells have the perovskite layer grown on top of an HTL, commonly PEDOT:PSS.[10] An ETL is then deposited on top, chosen to allow good band alignment without dissolving or reacting with the absorber layer. Each of these layers plays a key role in the functionality of the overall device. Dependant on the choice of p–i–n or n–i–p configuration, the perovskite absorber material needs to be deposited on either the hole transporting material, or the electron transporting material. The reported literature on n–i–p configuration shows variation in the fabrication processes and type of ETL used, and many efforts have focused on improving the ETL itself or the interface between the ETL and the perovskite. This also includes the use of interlayers to ensure that there is a gradual stepwise change in energy alignment heading towards the electrodes. Ideally, the highest occupied molecular orbital (HOMO) of the electron transport layer should be close to that of the perovskite, but slightly lower than that of the HTL. Similarly, the lowest unoccupied molecular orbital (LUMO) of the perovskite should be close to, but slightly higher then, that of the HTL.[11] Interlayers (ILs) can help to achieve this by bridging the gap where there are large energy jumps.

Table 1 summarises efficiency and processing conditions of highly efficient $CsPbI_2Br$ solar cells in n–i–p configuration, recently reported in literature, using the three common inorganic ETLs: SnO_2, TiO_2 and ZnO. ETLs are deposited by various solution processing methods, and the perovskite is commonly annealed at low temperatures of around 160 °C or higher temperatures > 250 °C.

SnO_2 is a commonly used ETL with the $CsPbI_2Br$ perovskite, either in the form of a nanoparticle layer or as a compact layer. Amorphous SnO_2 films have also been explored and are reported to lead to exceptionally high open circuit voltage (V_{OC}), attributed to the morphological changes in the SnO_2 film and improved charge extraction due to aging of the ETL precursor solution.[19] Although film morphology was cited as a reason for the improvement, analysis was limited, with only topography shown in secondary electron images. Commercially available SnO_2 nanoparticles dispersion at desired dilution (5 wt%,[24] 3 wt%,[25] 2.5 wt%[26]) or with surface modifications have been widely used to form the ETL layer. Modifications include complexing with ethylenediaminetetraacetic acid (EDTA),[27,28] or addition of NaCl,[29] both with the intention of reducing agglomeration to produce a better dispersed and smoother layer. Another common choice of ETL is TiO_2, with proven electron extraction capability[30,31] and chemical stability.[32] TiO_2

is the ETL material used in the first reported solar cell using perovskites in 2009.[33] It is often annealed at high temperatures, as shown in Table 1, which does however make it unfavourable for plastic substrates, compared to other generally lower temperature produced ETLs. Many studies also reported use of a mesoporous TiO_2 layer for a mesoscopic perovskite solar cell (PSC) device structure.[34–36] However, this adds an additional layer and cost into the process. Some examples within the literature describe high efficiencies from TiO_2 ETL based $CsPbI_2Br$ devices, including a 17% efficient device with a mesoscopic structure using a rubidium-doped perovskite reported by Patil *et al.*,[37] or the 17.5% efficient device based on undoped $CsPbI_2Br$ and standard bath-deposited TiO_2 layer, reported by Liu *et al.*[15] To date, these reported efficiencies are the highest reported for this type of device. However, despite the successes of TiO_2, the drive towards lower cost ETLs has continued to drive explorations into other ETL materials. ZnO is one such ETL material that has gained more attention over the past year due to a useful bandgap and extraction capabilities.[38,39] However, it is a hygroscopic material, requiring careful handling when used with the moisture-sensitive $CsPbI_2Br$ perovskite material. Within the literature, there are a number of reports on using dopants in ZnO to help with further improved band alignment,[22,40] leading to higher efficiency cells. There is a correlation between performance and reduction in the roughness of the ZnO films, which translates into smoother perovskite films.[40]

It is important to note that in all the studies discussed above and compiled in Table 1, limited attention has been paid to how the ETLs impact the growth of the perovskite and dictate the nanoscale chemical, compositional and structural heterogeneities. Two potentially useful techniques to investigate the effect of these ETLs on perovskite growth, crystallisation and optoelectronic performance are electron backscatter diffraction (EBSD) and cathodoluminescence (CL) hyperspectral imaging in the scanning electron microscope (SEM). Some studies have been carried out exploring these techniques in perovskite solar cell research.[41–46] These, however, have largely focussed on how localised grain structures and boundaries influence the luminescence of the material, or impact on non-radiative recombination, as well as how different phases can cause variation in luminescence across samples. Notably, a study by Chatterjee *et al.* showed how the emission of all-inorganic perovskite nanorods changed as the halide composition is altered, showcasing the adaptability of the growth method for synthesis of nanorods with emission over the entire visible light spectrum.[41] A study on perovskite films has shown the impact of ion segregation on the creation of species-rich regions in the sample, which influence the emission energy.[42] Monochromatic images showing specific emission wavelengths have been used to show areas of a film where iodide rich species are formed, segregated from the bulk film emission, leading to areas where absorption is affected, which in turn impacts device performance.[42] Examples of EBSD carried out on perovskite solar cells include the study by Schulz *et al.*,[43] where the technique was used to investigate specific protruding grains from a MAPI perovskite, identifying the grains as having differing orientation

This journal is © The Royal Society of Chemistry 2025

J. Mater. Chem. A, 2025, **13**, 11003–11014 | **11005**

to the bulk of the film, and linking this to significantly differing electrical properties. The overall perovskite structure in this case showed a large scale [110] orientation preference with respect to the sample normal.[43] There have been reports within the literature relating to the avoidance of the [110] orientation in $CsPbI_2Br$ perovskite layers, which is considered undesirable for device performance, as surface states in this orientation can affect light adsorption performance due to material energetics, as suggested in a study by Hu et al. The use of phenethyllammonium iodide (PEAI) dopant was explored to reduce preferred orientation along this direction from the surface of the perovskite film.[44]

Research combining luminescence and EBSD have proven to be effective in linking crystallographic orientation information to emission intensity. One such study using a flash annealing process focused on misorientation within individual grains. It was found that increasing the grain size in the films led to a greater spread in grain orientation, which correlated with reduced emission due to increased strain.[45] Such studies reveal features within the crystallographic mapping that are not visible through topography of the material, or by the PL/CL emission alone, highlighting the enhanced insights which the correlative measurements provide into the reason behind emission changes.[46]

In the present study, we investigate the effect of different electron transport layers—namely TiO_2, SnO_2 and ZnO—on the growth of $CsPbI_2Br$ perovskite thin films annealed at two different temperatures, and their resultant crystal orientation, by mapping localised and wider orientation effects using EBSD. Additionally, the impact of different orientations on the light emission from $CsPbI_2Br$ perovskite thin films is investigated by spectrally and spatially resolved CL. The EBSD and CL studies are supported by X-ray diffraction (XRD) analysis, to ensure both the localised EBSD effects and bulk crystal effects are revealed.

Experimental

Chemicals

PbI_2 (99.99%, trace metals basis) and $PbBr_2$ (99.98% trace metals basis) for perovskite precursors were acquired from TCI Chemicals. Dimethyl sulfoxide (99.8%+ extra dry), zinc acetate dihydrate (ACS Reagent ≥ 98%), titanium isopropoxide (99.999% trace metals basis) (TTIP), tin(IV) chloride pentahydrate (98%), caesium iodide (99.999% trace metals basis), ethanolamine (≥98% ACS Reagent) were purchased from Sigma-Aldrich. 2-Methoxyethanol (≥99.9% extra pure) and ethanol for use in TiO_2 production (99.5% absolute, extra dry) was acquired from Acros. Ethanol for use in SnO_2 was acquired from Fisher (≥99.8%, absolute, analytical reagent grade). Acetone and 2-propanol used for substrate cleaning were acquired from VWR chemicals and were of ≥99.5% and ≥99.7% purity respectively.

Precursor preparation

1.2 M $CsPbI_2Br$ precursor solution was made by the dissolution of 312.0 mg CsI, 277.7 mg PbI_2 and 220.0 mg $PbBr_2$ in 1 mL dimethylsulfoxide (DMSO). The solution was stirred in a vial holder for 1 hour at 60 °C, ensuring all powders were completely dissolved. The resultant solution was filtered through a 0.2 μm polytetrafluoroethylene (PTFE) filter. The ZnO sol–gel was prepared by dissolution of 400 mg zinc acetate in 4 mL 2-methoxyethanol and 110 μL ethanolamine, stirred overnight prior to deposition. The SnO_2 precursor solution was formed from 0.225 g $SnCl_2 \cdot 2H_2O$ dissolved in 10 mL absolute ethanol, stirred overnight. TiO_2 precursor was prepared from 2 vials, one containing 2.5 mL absolute ethanol and 300 μL titanium isopropoxide (TTIP), and another containing 2.5 mL absolute ethanol, to which 35 μL 2 M HCl was added outside the glovebox. The contents from acid containing vial was added to the TTIP containing vial. This completed the precursor for TiO_2. A polymethylmethacrylate (PMMA) precursor solution used for protective coating on $CsPbI_2Br$ films for XRD measurements was prepared by simple room temperature stirring of 10 mg PMMA in 1 mL chlorobenzene until dissolved.

Sample preparation

Pilkington TEC 15 FTO-coated glass substrates (2 cm × 1.5 cm) were cleaned with Hellmanex and sonicated subsequently in deionized water, 2-propanol and acetone. The substrates were then dried and plasma cleaned for 10 minutes prior to further processing. Electron transport layers were prepared by spin coating at 4000 rpm for 30 seconds for SnO_2, ZnO, or 2000 rpm for 1 minute for TiO_2, followed by annealing at 150 °C for 30 min for ZnO, 100 °C for 10 min then 180 °C for 1 hour for SnO_2, and 150 °C for 10 min then 500 °C for 30 min for TiO_2. These conditions were chosen and adapted from methods reported in the literature (Table 1). Just before the perovskite deposition, ETL coated substrates were annealed at 150 °C for 30 min (to remove any moisture), followed by UV/ozone cleaning for 10 min, and then immediately transferred to the glovebox. $CsPbI_2Br$ films were then deposited on the ETL coated substrates by static spin coating at 2000 rpm for 120 seconds, then annealing at 50 °C for 2 minutes, and final annealing at 160 °C for 10 minutes, for low temperature (LT) annealed samples, or 280 °C for 2 minutes for high temperature (HT) annealed samples. The samples were then allowed to cool to room temperature. For samples for XRD and other analyses in ambient air, a PMMA solution was spin coated on the samples at 2500 rpm for 20 seconds, prior to annealing at 100 °C for 10 minutes. This was used as a protective layer to prevent exposure to air for the length of analysis.

Cathodoluminescence hyperspectral imaging analysis

For CL analysis, $CsPbI_2Br$ films coated on different ETL layers were transferred from glovebox to SEM laboratory within an airtight box with silica beads. The samples were mounted on a pre-tilted rotatable specimen holder and loaded into the vacuum chamber. To limit image drift due to sample charging, silver paint was used to make an electrical contact to the surface of the film and areas near the silver paint were chosen for analysis. CL hyperspectral images were measured using an FEI Quanta 250 microscope with a bespoke CL system[47–49]

11006 | J. Mater. Chem. A, 2025, **13**, 11003–11014

This journal is © The Royal Society of Chemistry 2025

employing a 0.125 m focal length spectrograph with a 200 μm slit, a 500 nm blaze, 400 lines per mm ruled grating and an electron-multiplying CCD. The CL measurements were carried out in high vacuum ($\sim 1 \times 10^{-6}$ mbar) using 4 kV accelerating voltage and the hyperspectral images were taken across a 5 μm × 5 μm area, with a step size of 0.05 μm and an acquisition time per pixel of 50 ms.

Electron backscatter diffraction analysis

The EBSD measurements were performed using an Oxford Instruments Nordlys EBSD detector attached to the same SEM used for CL imaging. All measurements were performed at high vacuum, an accelerating voltage of 20 kV and a sample tilt of 70°. Dynamic focus and tilt correction were enabled. As for the CL, to limit image drift due to sample charging, silver paint was used to make an electrical contact to the surface of the film and areas near the silver paint were chosen for analysis. Multiple small-area high-resolution maps were taken of different areas, to investigate localised grain orientation effects. Further to this, one larger area scan with lower resolution was taken, to determine whether there are changes in preferential orientation across the sample, *i.e.* to assess the repeatability and uniformity across the sample. The size of the mapped area was altered between the high and low temperature samples, due to the difference in grain size observed for the samples. For the high temperature annealed samples, EBSD datasets were recorded from smaller areas of 12×12 μm^2 with a step size of 150 nm and from a larger area of 180×160 μm^2 with a step size of 2 μm. For the low temperature annealed samples, EBSD datasets were taken from small areas of 8×8 μm^2 with a step size of 100 nm and from a larger area of 180×160 μm^2 with a step size of 2 μm. The EBSD data, taken with a pattern resolution of 336×256 pixels, were indexed using Oxford Instruments' Refined Accuracy method. Initial indexing was performed using the CsPbBr$_3$ cubic phase structure, before being re-indexed using the CsPbI$_3$ cubic phase structure from the materials project.[50,51] Comparisons were made confirming that data was not altered by indexing using the different alloy combinations, concluding that a CsPbI$_3$ cubic phase structure was suitable for the analysis of CsPbI$_2$Br. The EBSD data was analysed using the MTEX toolbox using MATLAB.[52]

X-ray diffraction analysis

XRD measurements were performed on a Bruker D2 Phaser system with monochromatic Cu K$_\alpha$ radiation with a wavelength of 1.5406 Å. Samples scans were run for a 5–50° range with 0.04° increments on the 2θ scale. Throughout the measurement a rotation speed of 8 rpm was set for all samples.

Results

Plan-view topographic (secondary electron) SE imaging of the electron transport layers was performed to gain an overview of the general structure of these underlayers (Fig. S1†). From this we can note that all the layers show grain structure similar to that commonly observed for FTO substrates, confirming
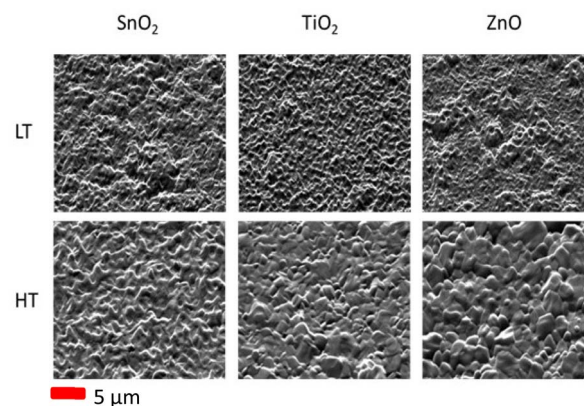

Fig. 1 SE images of the CsPbI$_2$Br perovskite grown at low temperature (LT 160 °C) and high temperature (HT, 280 °C) on different ETLs, tilted to 70° for EBSD.

a conformal coating over the underlying FTO film. For the CsPbI$_2$Br perovskite films grown on the respective ETLs, SE images were also taken prior to the EBSD analysis. SE images taken of the tilted perovskite samples (with tilt correction and dynamic focus applied) are shown in Fig. 1, with additional images taken top-down (zero sample tilt) are shown in the ESI (Fig. S2).† A top-down image gives an overall indication of the grain structure of the film, however when it is tilted to 70° for the EBSD, the surface roughness can be clearly seen. An increased grain size can be observed for the high temperature (HT) annealed perovskites, particularly in the case of a ZnO underlying layer, compared with low temperature (LT) prepared films. In the case of a SnO$_2$ underlayer, the structure looks similar in both cases, with the only difference when a higher temperature annealing is performed being a change in the apparent roughness of the film.

EBSD analysis was carried out on these samples to determine whether growth on differing ETLs, or changing annealing temperature of the perovskite, results in any variations in the structural homogeneity and preferential orientations in the perovskite films. Inverse pole figure (IPF) maps, shown in Fig. 2, were used to compare the orientation of the grains in the perovskite films grown on different ETLs and using different annealing temperatures. IPF maps show the crystallographic orientation/direction with respect to the sample reference frame directions X, Y and Z corresponding to the horizontal, vertical and sample normal directions, respectively. The crystallographic directions (or orientation) of grains are shown by the colour scale in the IPF map. With respect to the sample normal direction (Z direction), grains across all samples show a preference for the [100] direction (red grains), with some secondary preference for [110] (green grains), particularly observable in the low temperature annealed CsPbI$_2$Br films deposited on TiO$_2$ ETL. Fig. 2 shows the IPF maps with respect to Y and Z, with the X map included in the Fig. S5.† In the sample plane (*e.g.* IPF Y) a more random distribution of orientations is observed as seen by a range of differently coloured grains. White regions are where the data has not been indexed
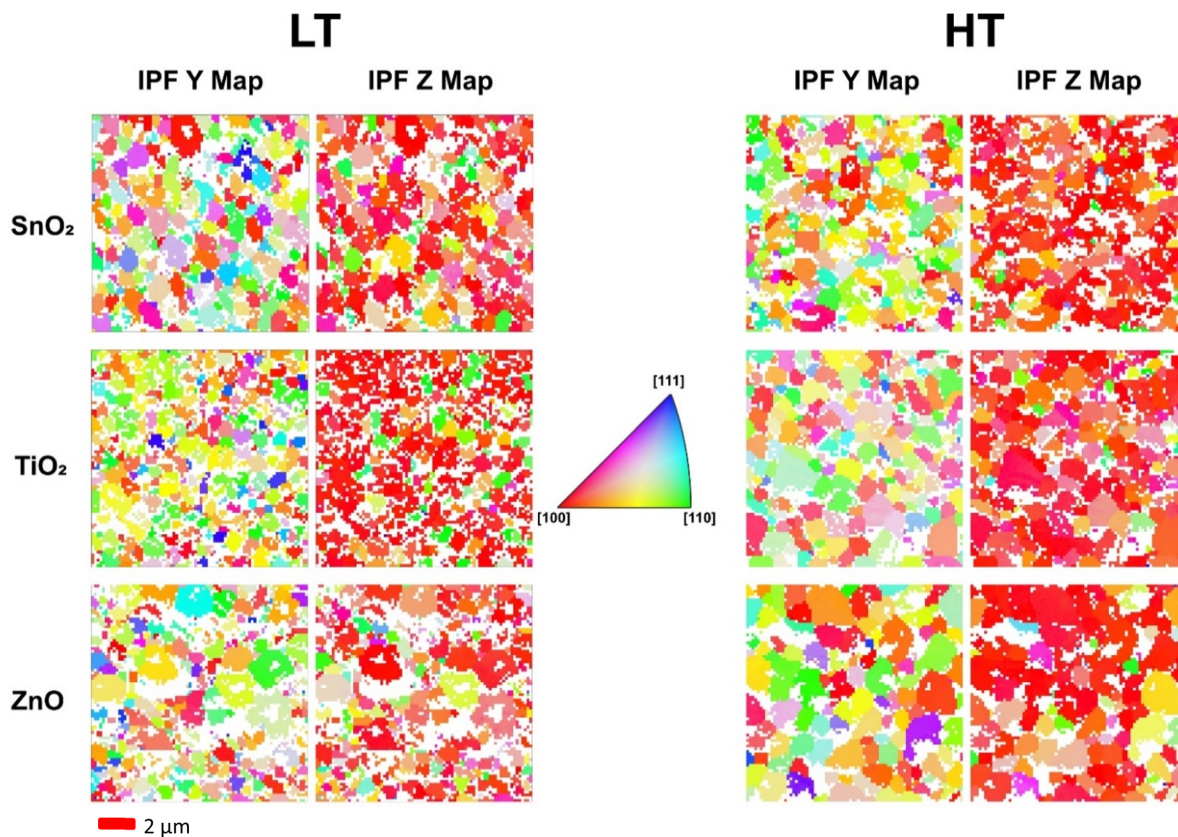
This journal is © The Royal Society of Chemistry 2025

J. Mater. Chem. A, 2025, **13**, 11003–11014 | **11007**

Fig. 2 Inverse pole figure maps with respect to Y and Z directions for $CsPbI_2Br$ grown with the low temperature (160 °C, LT) and high temperature (280 °C, HT) annealing on the different ETLs (SnO_2, TiO_2 and ZnO).

due to poor signal-to-noise ratio as a result of shadowing of regions of the film due to changes in sample topography and poor-quality patterns at grain boundaries. Table 2 below compares the number of indexed pixels in the EBSD maps. There is an increase in the percentage of pixels indexed for the high temperature annealed perovskite films (as compared to the low temperature annealed films) grown on the TiO_2 and ZnO ETLs, but not for that grown on the SnO_2 ETL.

The high temperature annealing of perovskite grown on the TiO_2 substrate allowed the grains to reorient into a preferred [100] direction in Z, the sample normal, reducing the preference towards [110] seen by the schematically green coloured grains in the low temperature annealed sample (Fig. 2), and this is supported by a reduction in intensity of the [110] central spot in the Fig. 4 pole figures shown later. One can also note from Fig. 2 that there are smaller grains in the $CsPbI_2Br$ film grown on TiO_2 at low temperature. The $CsPbI_2Br$ grains on TiO_2 are enlarged when annealed at high temperature, but remain smaller than those on the ZnO ETL.

Band contrast maps can be used to help visualise the grain structure and for the rough estimation of grain sizes. A band contrast map is a measure of the quality of the Kikuchi patterns, with low intensity obtained where indexing is not possible due to no acquisition of patterns or acquisition of poor patterns, for example due to shadowing as a result of surface topography, and at grain boundaries. IPF maps, in addition to band contrast maps, can be used to estimate how the grain size changes across different samples. A difference in grain size is far more observable when comparing the two annealing temperatures, as opposed to between different ETLs within one temperature sample set. Comparison of the band contrast maps for the samples grown at both the high and low temperatures reveals these changes, as displayed in Fig. 3.

The ZnO samples displayed the largest increase in grain size and most of the grains appear to be of similar size when annealed at higher temperatures; this contrasts with the films annealed at lower temperatures, where the maps show very small grains between some larger ring-shaped grains. For the TiO_2 ETL sample, the grain size increased, whereas only a very

Table 2 EBSD indexing statistics

	LT SnO_2	LT TiO_2	LT ZnO	HT SnO_2	HT TiO_2	HT ZnO
% pixels indexed	72%	65%	64%	72%	80%	79%

11008 | *J. Mater. Chem. A*, 2025, **13**, 11003–11014

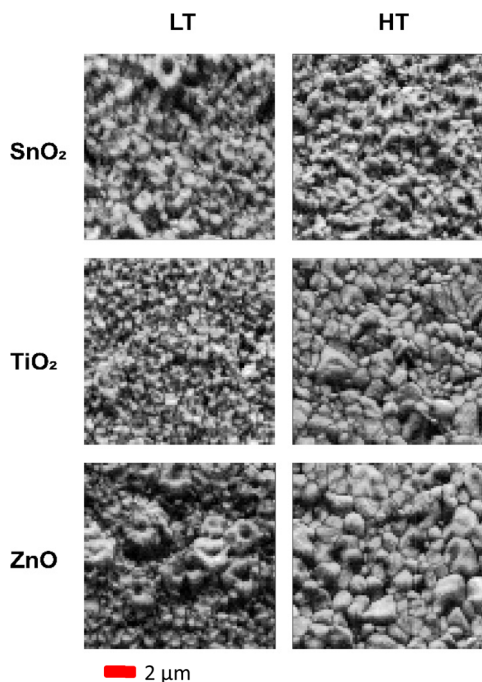This journal is © The Royal Society of Chemistry 2025

Fig. 3 The comparison of band contrast maps of CsPbI$_2$Br perovskite film annealed at low temperature (LT, 160 °C) and high temperature (HT, 280 °C).

minor change in grain size was observed for the SnO$_2$ ETL case. It is important to note that the sensitivity of these materials to the electron beam provides a challenge to the recording of large detailed maps for high statistical confidence. Additionally, the Kikuchi patterns near and at the grain boundaries are of lower quality, which prevents the indexing of the patterns in areas shown white in the IPF maps (Fig. 2). Grain sizes were estimated from the band contrast maps using ImageJ,[53] with a selection of 10 of the clearest grains in the sample and averaging across length and breadth, to give an estimated range of grain sizes for the samples grown at high temperature. For the low temperature annealed films, as the grain boundaries are not well defined, it is challenging to estimate grain size from the band contrast maps. Samples grown on ZnO and TiO$_2$ at high temperature have grains in the approximate range of 1400–2350 nm and 750–1450 nm, respectively, whereas in the case of a film grown on SnO$_2$, the grains are visibly smaller and indistinguishable.

Pole figures give overall orientation information across the entire sample area and have been constructed using data recorded over a large area to provide good statistics. Pole figures for the [100] and [110] directions from all samples are shown in Fig. 4. All samples display the distinct preferential orientation in [100] as evidenced by the most intense spot in the centre of the [100] pole figure. The [110] spot intensity is lower in all cases
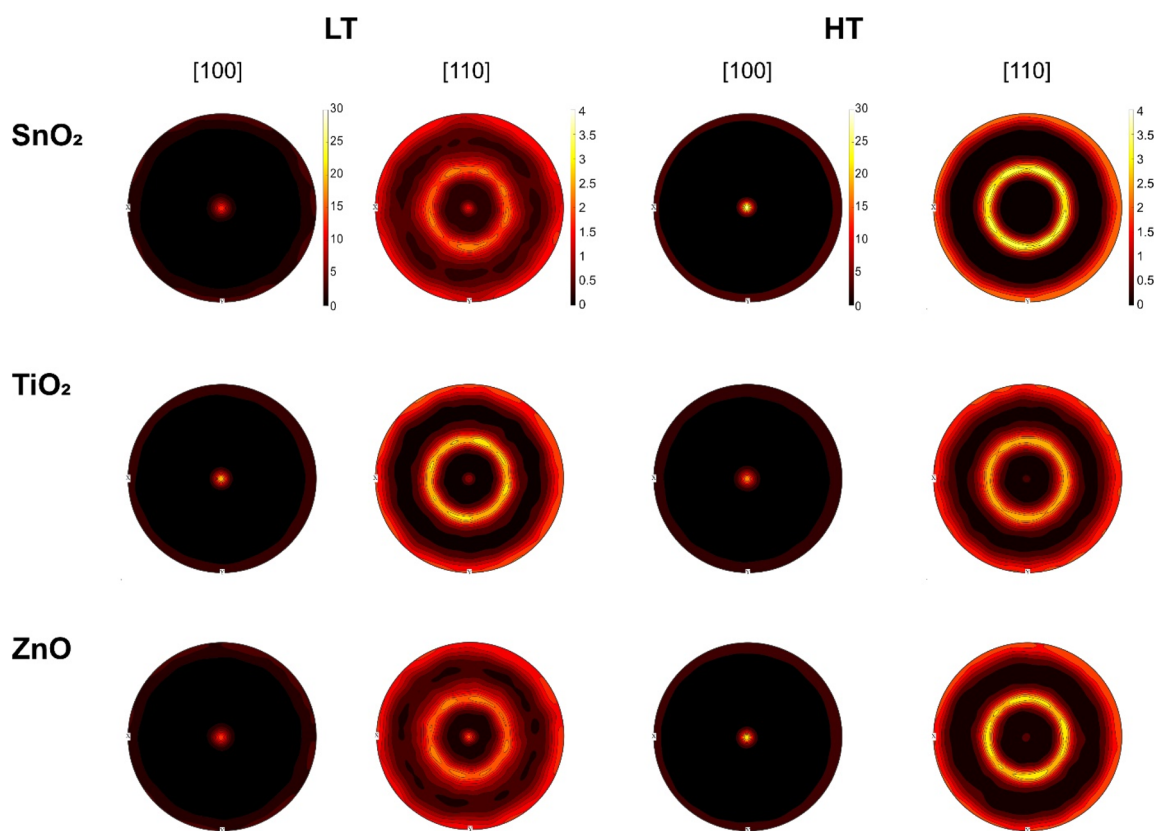

Fig. 4 Comparison of stereographic projection pole figures showing upper hemisphere for the [100] and [110] directions, for the CsPbI$_2$Br films on different ETLs and annealed at low temperature (LT, 160 °C) and high temperature (HT, 280 °C). Note the different intensity scale bars for the [100] and [110] pole figures.

This journal is © The Royal Society of Chemistry 2025

J. Mater. Chem. A, 2025, **13**, 11003–11014 | **11009**

in the high temperature samples, showing that the high temperature preparation route enhances the preferential orientation of the samples. Full comparisons of the pole figures, secondary electron images before and after EBSD measurements, and the IPF maps including along the X plane are given in the ESI, Fig. S3–S5.†

Mapping of the FTO substrates was also attempted by EBSD, however the Kikuchi pattern quality was very low, grain size very small, and the substrates could not be successfully measured. XRD analysis of the samples was carried out to confirm the conclusions from the EBSD. The XRD patterns in Fig. 5 show clear, strong (100) and (200) peaks confirming the preferred (100) orientation in the cubic phase CsPbI$_2$Br films. All samples showed a limited presence of (110) orientation as observed in the EBSD, revealing the polycrystalline nature of the films. However, it is notable that the film deposited on TiO$_2$ and annealed at high temperature exhibits a significant shift of the XRD peaks towards higher angles (in contrast to the one grown at low temperature), followed by that grown on SnO$_2$ which shows a relatively smaller shift, whereas no shift was observed for film grown on ZnO. This shift could be linked to additional strain within the CsPbI$_2$Br films when the sample is annealed at high temperatures, due to the difference in thermal expansion coefficient of the perovskite and the ETLs.[54] When the CsPbI$_2$Br film formed at high temperature and then cools to room temperature, it contracts owing to its positive thermal expansion coefficient (α). However, since the CsPbI$_2$Br films are deposited on substrates with a lower α [perovskite $\sim$ 3–8.4 $\times$ 10^{-5} K^{-1}, TiO$_2$ $\sim$ 8–11 $\times$ 10^{-6} K^{-1}, SnO$_2$ $\sim$ 3–8 $\times$ 10^{-6} K^{-1}, ZnO $\sim$ 1–2 $\times$ 10^{-5} K^{-1}],[55–57] the contact between the film and the substrate limits the perovskite from contracting when it cools back to room temperature after the high temperature annealing. This leads to a tensile strain along the in-plane directions and a simultaneous compressive strain in the out-of-plane direction due to the positive Poisson's ratio in the perovskites. A shift to higher angles in XRD for the out-of-plane direction has been observed for compressive strain.[58] Since $\Delta\alpha$ is higher for SnO$_2$ and TiO$_2$ than for ZnO, we would expect higher shifts in the XRD peaks for films grown on SnO$_2$ and TiO$_2$ than those on ZnO, which is in reasonable agreement with the observation in the present study. Additionally, lattice strain will also arise at the interface between the perovskite and the ETLs due the lattice mismatch between the two layers. The observed XRD shifts can thus be elucidated as due to an interplay between the thermal and lattice mismatch between the perovskite and the ETLs.

The stress present within the CsPbI$_2$Br films due to the difference in thermal expansion coefficients, dependant on the annealing temperature and the underlying ETL material, can be calculated by using the following formula[59]

$$\sigma_{\Delta T} = \frac{E_p}{1 - \nu_p}(\alpha_s - \alpha_p)\Delta T$$

The value is calculated for a range of annealing temperatures, taking the modulus of the perovskite (E_p) to be 10 GPa,[60] Poisson's ratio ν_p in the perovskite to be 0.3,[61] and the thermal expansion coefficients of the materials to be the highest value from the ranges reported in literature. α_s and α_p are the thermal expansion coefficients of the relevant ETL (ZnO/TiO$_2$/SnO$_2$) and the perovskite absorber material CsPbI$_2$Br, respectively. Plotting the calculated values of the stress *versus* annealing temperature of the perovskite grown on each of the ETLs (Fig. 6), it can be noted that the SnO$_2$ introduces the highest level of thermally induced stress in the perovskite film, followed by the TiO$_2$, then
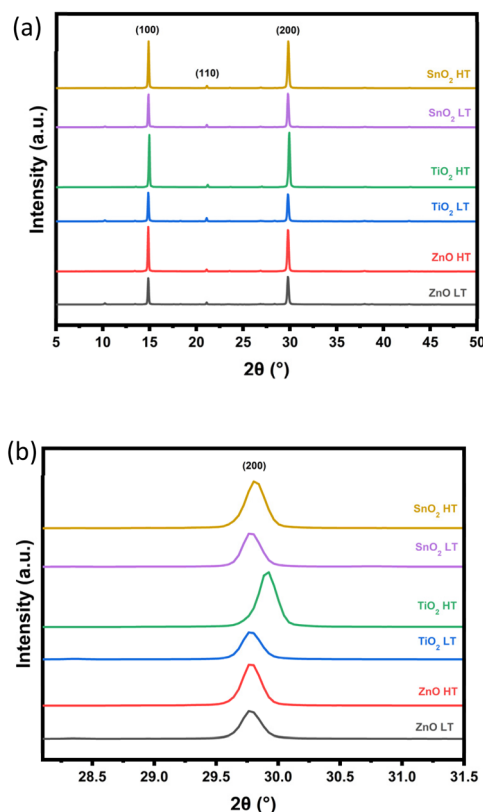

Fig. 5 (a) XRD plot for CsPbI$_2$Br films grown on top of three different ETLs – SnO$_2$, TiO$_2$ and ZnO, annealed at low temperature (LT, 160 °C) and high temperature (HT, 280 °C), (b) magnified (200) peak for all the samples.
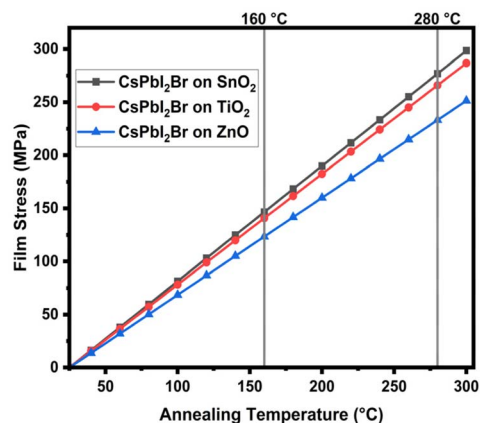

Fig. 6 Plot of film stress in samples of all-inorganic CsPbI$_2$Br grown atop the three different ETL's – SnO$_2$, TiO$_2$ and ZnO as function of the annealing temperature.

11010 | *J. Mater. Chem. A*, 2025, **13**, 11003–11014

This journal is © The Royal Society of Chemistry 2025

followed by the ZnO. This can be correlated with the grain sizes observed in the CsPbI$_2$Br films grown on different ETLs in this study. Cathodoluminescence hyperspectral imaging experiments were conducted on the perovskite films to determine whether the structural changes in the film resulted in variations in the light-emitting properties of the film. Fig. 7 shows CL maps of the centroid wavelength (a statistical measure of the wavelength shift extracted from the full spectrum recorded at

each pixel), along with secondary electron images, for CsPbI$_2$Br films annealed at 160 °C (LT) and 280 °C (HT). Variation is observed in the emission across the samples, from the expected value of 650 nm reported in the literature.[20,62] This is linked to heterogeneities and misorientations in the films, leading to strain being induced in the absorber in those samples.[63] Considering the CsPbI$_2$Br films grown on SnO$_2$ it is notable that both in high and low temperature annealed perovskite films,
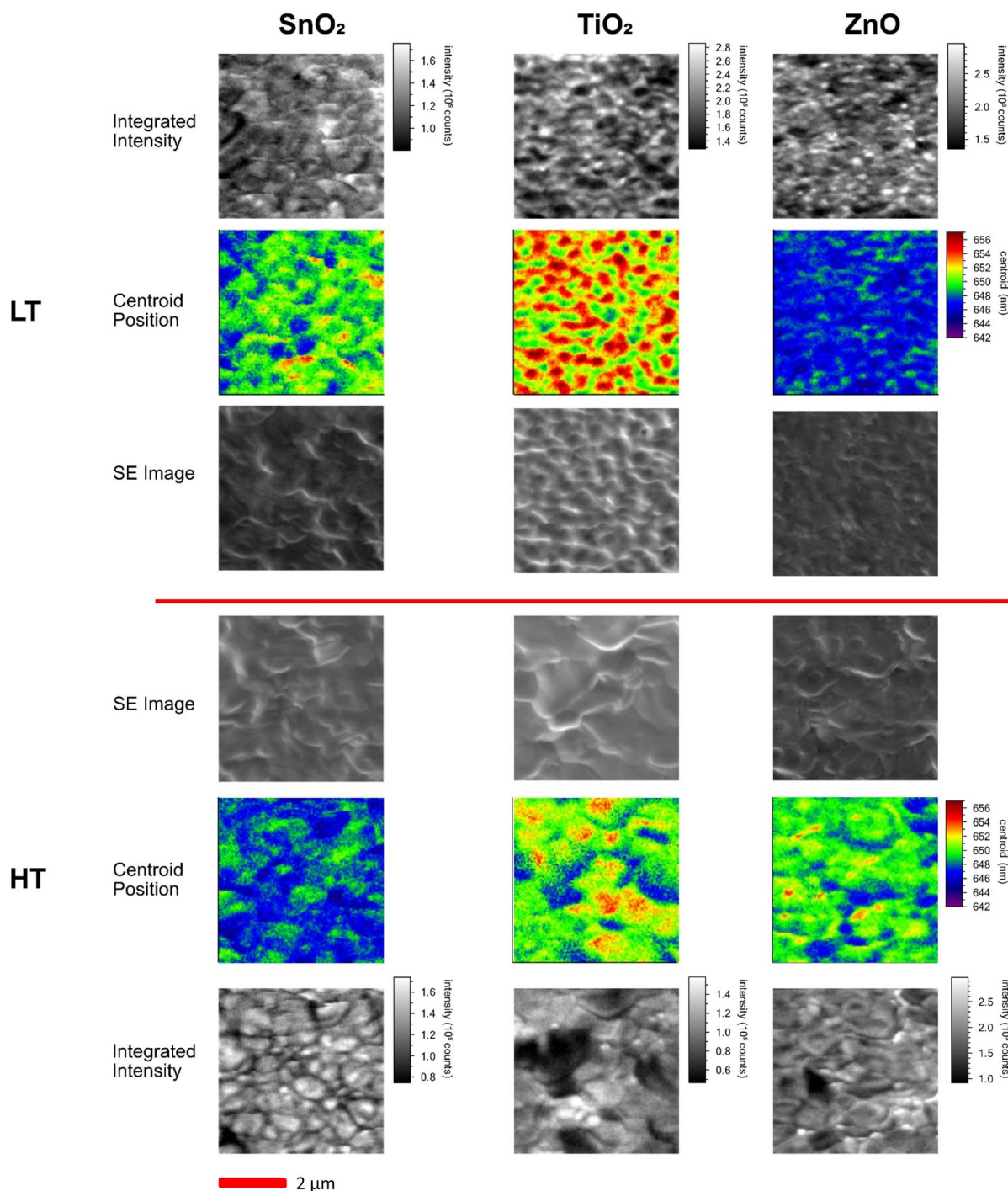

Fig. 7 Maps of CL centroid wavelength (colour), CL intensity (greyscale) and secondary electron images (greyscale) of the mapped region of CsPbI$_2$Br films grown on the differing ETLs (SnO$_2$, TiO$_2$, and ZnO) and annealed at low temperature (LT, 160 °C) and high temperature (HT, 280 °C). Scales are identical throughout.

This journal is © The Royal Society of Chemistry 2025

J. Mater. Chem. A, 2025, **13**, 11003–11014 | **11011**

the nature of emission from the films stays relatively the same. There is clear heterogeneity within the sample grown on TiO_2 at low temperature, however this is reduced (and becomes similar to the SnO_2 reference) when annealed at high temperature. On the other hand, there is a major emission peak shift revealed in ZnO when one moves from annealing at 160 °C to 280 °C, as can be seen by the change in predominant colour from blue to red/green on the centroid wavelength scale. In both ZnO samples there is an improved level of homogeneity relative to the TiO_2 low temperature sample. The redshift could be resultant of some change to the film either by morphological change such as the large grain growth (seen in the EBSD earlier), or due to release of moisture, related to the hygroscopic nature of ZnO. All samples show reduced heterogeneity when prepared at the higher temperature. Shifts within the film, particularly in the low temperature TiO_2 case, could be related to localised compositional changes as reported previously in literature,[63] however all films were deposited using the same precursor under same ambient conditions within the nitrogen glovebox and so should have the same overall composition. As mentioned earlier, it is suggested that there could be some strain effects in the film. The effect is not observed on the other ETLs.

In the integrated CL intensity plots, it is notable that signal has fewer dark regions in the films on ZnO ETL, in contrast to the film on TiO_2 which shows a more variable behaviour with large areas of reduced CL signal. These large dark areas shown in the films grown-on TiO_2 sample suggest large defects where losses will occur from the solar cells, affecting efficiency. The large grain structure seen in the high temperature sample grown on ZnO (as shown in EBSD), combined with the uniform CL seen here, is desirable, as reduced numbers of grain boundaries lead to lower losses and higher efficiencies.

Conclusions

The role of the electron transport layer in defining the growth of perovskite films has been revealed, showing a significant dependence on the correct choice of underlayer for grain size, orientation and the crystal quality. The large-scale grain growth seen within the high temperature processed $CsPbI_2Br$ perovskite grown on ZnO reveals this as a suitable choice of transport layer. In addition, the ZnO layer can be prepared at reduced temperatures compared to TiO_2, a positive step towards cost-effective commercial viability of perovskite solar cells and application to temperature-sensitive substrates. The results of this work show that the structure of the electron transport layer must be considered fundamental when designing perovskite solar cell architecture, as this can effect the stability and performance, alongside the commercial and environmental implications.

Data availability

All data underpinning this publication are openly available from the University of Strathclyde at **https://doi.org/10.15129/7050fbb9-c8b1-4e52-9939-2a8765e6f2ec**.

Author contributions

SN carried out and analysed most of the practical work and drafted the manuscript. JB carried out EBSD measurements and helped in data analysis with the support of CTC. PRE provided advice and training for CL and CL data analysis. AI conceptualised the work. AI and RWM supervised the work and helped in results interpretation. All the authors provided inputs to the manuscript.

Conflicts of interest

The authors declare that there are no conflicts of interest that could appear to have influence on the work presented in this paper.

Acknowledgements

Notes and references

1 Web of Science Search Conducted 23/04/2024 'Perovskite and Solar'.

2 H. Min, D. Y. Lee, J. Kim, G. Kim, K. S. Lee, J. Kim, M. J. Paik, Y. K. Kim, K. S. Kim, M. G. Kim, T. J. Shin and S. I. Seok, *Nature*, 2021, **598**, 444–450.

3 T. Zhang, X. Meng, Y. Bai, S. Xiao, C. Hu, Y. Yang, H. Chen and S. Yang, *J. Mater. Chem. A*, 2017, **5**, 1103–1111.

4 G. Abdelmageed, C. Mackeen, K. Hellier, L. Jewell, L. Seymour, M. Tingwald, F. Bridges, J. Z. Zhang and S. Carter, *Sol. Energy Mater. Sol. Cells*, 2018, **174**, 566–571.

5 Y. A. Olanrewaju, K. Orisekeh, O. V. Oyelade, R. K. Koech, R. Ichwani, A. I. Ebunu, D. I. Amune, A. Bello, V. C. Anye, O. K. Oyewole and W. O. Soboyejo, *AIP Adv.*, 2022, **12**, 015122.

6 Z. Guo, A. K. Jena, I. Takei, M. Ikegami, A. Ishii, Y. Numata, N. Shibayama and T. Miyasaka, *Adv. Funct. Mater.*, 2021, **31**, 2103614.

7 S. Xie, R. Xia, Z. Chen, J. Tian, L. Yan, M. Ren, Z. Li, G. Zhang, Q. Xue, H. L. Yip and Y. Cao, *Nano Energy*, 2020, **78**, 105238.

8 X. Ding, M. Cai, X. Liu, Y. Ding, X. Liu, Y. Wu, T. Hayat, A. Alsaedi and S. Dai, *ACS Appl. Mater. Interfaces*, 2019, **11**, 37720–37725.

9 S. Ullah, J. Wang, P. Yang, L. Liu, S.-E. Yang, T. Xia, H. Guo and Y. Chen, *Mater. Adv.*, 2021, **2**, 646–683.

10 Y. Xia, G. Yan and J. Lin, *Nanomaterials*, 2021, **11**, 3119.

11012 | *J. Mater. Chem. A*, 2025, **13**, 11003–11014

This journal is © The Royal Society of Chemistry 2025

11 N. Lu, C. Zhou, Y. Wang, A. M. Elquist, A. Ghods, I. T. Ferguson and V. G. Saravade, in *Oxide-based Materials and Devices IX*, ed. F. H. Teherani, D. C. Look and D. J. Rogers, SPIE, 2018, p. 53.

12 P. Fu, Z. Liu, D. Xu, B. Yang, Y. Liu, Z. Feng, Z. Feng, X. Guo and C. Li, *Sol. RRL*, 2022, 2101057.

13 W. Tang, Y. Chen, J. Yang, R. Yuan, Y. Lv, Q. Ma, Y. Wu, P. Zhang and W.-H. Zhang, *J. Power Sources*, 2021, **482**, 228965.

14 W. Chen, H. Chen, G. Xu, R. Xue, S. Wang, Y. Li and Y. Li, *Joule*, 2019, **3**, 191–204.

15 X. Liu, H. Lian, Z. Zhou, C. Zou, J. Xie, F. Zhang, H. Yuan, S. Yang, Y. Hou and H. G. Yang, *Adv. Energy Mater.*, 2022, **12**, 2103933.

16 S. S. Mali, J. V. Patil, P. S. Shinde, G. de Miguel and C. K. Hong, *Matter*, 2021, **4**, 635–653.

17 H. Zhang, J. Zhuang, X. Liu, Z. Ma, H. Guo, R. Zheng, S. Zhao, F. Zhang, Z. Xiao, H. Wang and H. Li, *J. Mater. Sci. Technol.*, 2021, **82**, 40–46.

18 Y. Zhang, C. Wu, D. Wang, Z. Zhang, X. Qi, N. Zhu, G. Liu, X. Li, H. Hu, Z. Chen, L. Xiao and B. Qu, *Sol. RRL*, 2019, **3**, 1–8.

19 Z. Guo, A. K. Jena, I. Takei, G. M. Kim, M. A. Kamarudin, Y. Sanehira, A. Ishii, Y. Numata, S. Hayase and T. Miyasaka, *J. Am. Chem. Soc.*, 2020, **142**, 9725–9734.

20 A. Wang, J. Wang, X. Niu, C. Zuo, F. Hao and L. Ding, *InfoMat*, 2022, **4**, e12263.

21 J. Ma, M. Qin, Y. Li, T. Zhang, J. Xu, G. Fang and X. Lu, *J. Mater. Chem. A*, 2019, **7**, 27640–27647.

22 Z. Xu, X. Liu, S. Fu, J. Wang, J. Zhang, L. Huang, Z. Hu and Y. Zhu, *Appl. Phys. Lett.*, 2021, **119**, 212101.

23 P. Wang, H. Wang, Y. Mao, H. Zhang, F. Ye, D. Liu and T. Wang, *Adv. Sci.*, 2020, **7**, 2000421.

24 J. Ma, Z. Lin, X. Guo, L. Zhou, J. He, Z. Yang, J. Zhang, Y. Hao, S. Liu and J. Chang, *J. Energy Chem.*, 2021, **63**, 558–565.

25 S. Zhang, H. Gu, S.-C. Chen and Q. Zheng, *J. Mater. Chem. C*, 2021, **9**, 4240–4247.

26 Y. Hu, L. Cai, Z. Xu, Z. Wang, Y. Zhou, G. Sun, T. Sun, Y. Qi, S. Zhang and Y. Tang, *Inorg. Chem.*, 2023, **62**, 5408–5414.

27 S. Wang, H. Sang, Y. Jiang, Y. Wang, Y. Xiong, Y. Yu, R. He, B. Chen, X. Zhao and Y. Liu, *ACS Appl. Mater. Interfaces*, 2021, **13**, 48555–48568.

28 D. Yang, R. Yang, K. Wang, C. Wu, X. Zhu, J. Feng, X. Ren, G. Fang, S. Priya and S. Liu, *Nat. Commun.*, 2018, **9**, 3239.

29 C. C. Lin, T. N. Murakami, M. Chikamatsu, T. Bessho, M. Furue and H. Segawa, *ACS Omega*, 2021, **6**, 17880–17889.

30 B. Wang, M. Zhang, X. Cui, Z. Wang, M. Rager, Y. Yang, Z. Zou, Z. L. Wang and Z. Lin, *Angew. Chem., Int. Ed.*, 2020, **59**, 1611–1618.

31 X. Shi, Y. Ding, S. Zhou, B. Zhang, M. Cai, J. Yao, L. Hu, J. Wu, S. Dai and M. K. Nazeeruddin, *Adv. Sci.*, 2019, **6**, 1901213.

32 A. Raj, M. Kumar, A. Kumar, A. Laref, K. Singh, S. Sharma and A. Anshul, *Mater. Lett.*, 2022, **313**, 131692.

33 A. Kojima, K. Teshima, Y. Shirai and T. Miyasaka, *J. Am. Chem. Soc.*, 2009, **131**, 6050–6051.

34 Y. Rong, L. Liu, A. Mei, X. Li and H. Han, *Adv. Energy Mater.*, 2015, **5**, 1501066.

35 W. Xiang, Z. Wang, D. J. Kubicki, W. Tress, J. Luo, D. Prochowicz, S. Akin, L. Emsley, J. Zhou, G. Dietler, M. Grätzel and A. Hagfeldt, *Joule*, 2019, **3**, 205–214.

36 S. R. Rondiya, S. Mali, A. Roy, G. K. Inwati, G. K. Rahane, Y. A. Jadhav, S. Suresh, T. Debnath, C. K. Hong and N. Y. Dzade, *Phys. Chem. Chem. Phys.*, 2023, 29050–29060.

37 J. V. Patil, S. S. Mali and C. K. Hong, *Sol. RRL*, 2020, **4**, 1–9.

38 X. Zhang, D. Zhang, T. Guo, J. Zou, J. Jin, C. Zheng, Y. Zhou, Z. Zhu, Z. Hu, Q. Cao, S. Wu, J. Zhang and Q. Tai, *J. Mater. Chem. A*, 2023, 9616–9625.

39 Y. Li, Y. Zhang, P. Zhu, J. Li, J. Wu, J. Zhang, X. Zhou, Z. Jiang, X. Wang and B. Xu, *Adv. Funct. Mater.*, 2023, 2309010.

40 J. Li, J. Yang, J. Ma, J. Liang, Y. Liu, X. Hu, C. Chen, W. Yang, J. Min, Q. Bao, G. Fang and C. Tao, *Chem. Eng. J.*, 2021, **417**, 129247.

41 T. Paul, B. K. Chatterjee, S. Maiti, S. Sarkar, N. Besra, B. K. Das, K. J. Panigrahi, S. Thakur, U. K. Ghorai and K. K. Chattopadhyay, *J. Mater. Chem. C*, 2018, **6**, 3322–3333.

42 O. Hentz, Z. Zhao and S. Gradečak, *Nano Lett.*, 2016, **16**, 1485–1490.

43 T. Leonhard, A. D. Schulz, H. Röhm, S. Wagner, F. J. Altermann, W. Rheinheimer, M. J. Hoffmann and A. Colsmann, *Energy Technol.*, 2019, **7**, 1800989.

44 W. Hu, F. Si, Y. Yang, H. Xue, W. Li, J. Hu and F. Tang, *Chem. Phys.*, 2022, **562**, 111651.

45 S. Jariwala, H. Sun, G. W. P. Adhyaksa, A. Lof, L. A. Muscarella, B. Ehrler, E. C. Garnett and D. S. Ginger, *Joule*, 2019, **3**, 3048–3060.

46 S. Nicholson, J. Bruckbauer, P. R. Edwards, C. Trager-Cowan, R. W. Martin and A. Ivaturi, *J. Mater. Chem. A*, 2024, **12**, 25131–25139.

47 C. Trager-Cowan, A. Alasmari, W. Avis, J. Bruckbauer, P. R. Edwards, G. Ferenczi, B. Hourahine, A. Kotzai, S. Kraeusel, G. Kusch, R. W. Martin, R. McDermott, G. Naresh-Kumar, M. Nouf-Allehiani, E. Pascal, D. Thomson, S. Vespucci, M. D. Smith, P. J. Parbrook, J. Enslin, F. Mehnke, C. Kuhn, T. Wernicke, M. Kneissl, S. Hagedorn, A. Knauer, S. Walde, M. Weyers, P.-M. Coulon, P. A. Shields, J. Bai, Y. Gong, L. Jiu, Y. Zhang, R. M. Smith, T. Wang and A. Winkelmann, *Semicond. Sci. Technol.*, 2020, **35**, 054001.

48 L. K. Jagadamma, P. R. Edwards, R. W. Martin, A. Ruseckas and I. D. W. Samuel, *ACS Appl. Energy Mater.*, 2021, **4**, 2707–2715.

49 P. R. Edwards, L. K. Jagadamma, J. Bruckbauer, C. Liu, P. Shields, D. Allsopp, T. Wang and R. W. Martin, *Microsc. Microanal.*, 2012, **18**, 1212–1219.

50 A. Jain, S. P. Ong, G. Hautier, W. Chen, W. D. Richards, S. Dacek, S. Cholia, D. Gunter, D. Skinner, G. Ceder and K. A. Persson, *APL Mater.*, 2013, **1**, 011002.

51 Data retrieved from the Materials Project for CsPbI3 (mp-1069538) from database version v2021.11.10.

52 F. Bachmann, R. Hielscher and H. Schaeben, *Solid State Phenom.*, 2010, **160**, 63–68.

This journal is © The Royal Society of Chemistry 2025

J. Mater. Chem. A, 2025, **13**, 11003–11014 | **11013**

53 C. A. Schneider, W. S. Rasband and K. W. Eliceiri, *Nat. Methods*, 2012, **9**, 671–675.

54 W. Hui, Y. Xu, F. Xia, H. Lu, B. Li, L. Chao, T. Niu, B. Du, H. Du, X. Ran, Y. Yang, Y. Xia, X. Gao, Y. Chen and W. Huang, *Nano Energy*, 2020, **73**, 104803.

55 M. Singh and M. Singh, *Nanosci. Nanotechnol. Res.*, 2013, **1**, 27–29.

56 D. R. Hummer, P. J. Heaney and J. E. Post, *Powder Diffr.*, 2007, **22**, 352–357.

57 J. Wang, H. L. Li and M. H. Liu, *Adv. Mater. Res.*, 2012, **591–593**, 965–968.

58 B. Yang, D. Bogachuk, J. Suo, L. Wagner, H. Kim, J. Lim, A. Hinsch, G. Boschloo, M. K. Nazeeruddin and A. Hagfeldt, *Chem. Soc. Rev.*, 2022, **51**, 7509–7530.

59 D.-J. Xue, Y. Hou, S.-C. Liu, M. Wei, B. Chen, Z. Huang, Z. Li, B. Sun, A. H. Proppe, Y. Dong, M. I. Saidaminov, S. O. Kelley, J.-S. Hu and E. H. Sargent, *Nat. Commun.*, 2020, **11**, 1514.

60 N. Rolston, K. A. Bush, A. D. Printz, A. Gold-Parker, Y. Ding, M. F. Toney, M. D. McGehee and R. H. Dauskardt, *Adv. Energy Mater.*, 2018, **8**, 1802139.

61 Y. Wang, C. Xie, X. Yao, Q. Chen, W. Liu, Y. Fu, Q. Liu, J. Li, Y. Li and D. He, *J. Materiomics*, 2022, **8**, 358–365.

62 J. Wu, S.-C. Liu, Z. Li, S. Wang, D.-J. Xue, Y. Lin and J.-S. Hu, *Natl. Sci. Rev.*, 2021, **8**, nwab047.

63 X. Luo, W. Xu, G. Zheng, S. Tammireddy, Q. Wei, M. Karlsson, Z. Zhang, K. Ji, S. Kahmann, C. Yin, Y. Zou, Z. Zhang, H. Chen, L. A. B. Marçal, H. Zhao, D. Ma, D. Zhang, Y. Lu, M. Li, C. Deibel, S. D. Stranks, L. Duan, J. Wallentin, W. Huang and F. Gao, *Matter*, 2024, **7**, 1054–1070.